ORIGINAL ARTICLE

lajss.org© Latin American Journal of Solids and Structures

www.lajss.org

Dynamic response of projectile and charge during penetration into concrete target with high velocity

Changlin Zhu[a], Chuang Liu[a]*, Qiang Sheng[a], Yuxuan Deng[a], Xiaoming Wang[a]

[a]School of Mechanical Engineering, Nanjing University of Science and Technology, Nanjing 210094, China. Email: zhuchanglin@njust.edu.cn, chuang.liu@njust.edu.cn, 3581368151@qq.com, denyuxuan103@163.com, 202xm@163.com

* Corresponding author

https://doi.org/10.1590/1679-7825/e8546

Abstract

To study the dynamic response characteristics of the penetrating warhead under the impact load, experiments of projectile penetration into a concrete target were performed based on a 30-mm ballistic gun. Penetration resistance model of the projectile penetration into the concrete target was modified by considering the wake separation and cratering effects associated with oblique penetration. The projectile deformation process during penetration was analyzed by the modified penetration model and validated by experimental results. In particular, the deformation, stress, and strain distribution characteristics of the projectile and charge were analyzed. Results show that during oblique penetration of the target by the projectile, the nose of projectile endures substantial compressive forces due to the compression wave. This results in considerable deformation within a region spanning from 0.32 to 0.59 times the projectile's length from the nose. Additionally, a coupling effect of compression and tension waves induces significant transverse deformation at the projectile's tail, spanning from 0.88 to 1.0 times the projectile's length from the tail end.

Keywords

Penetration, Dynamic response, Concrete-target, Numerical calculation

Graphical Abstract

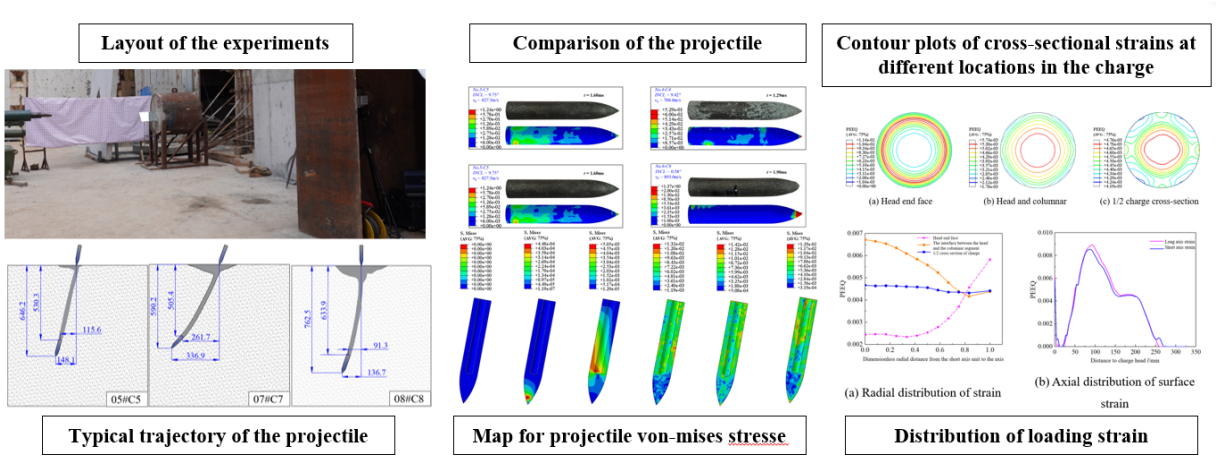

1 INTRODUCTION

The application of high-strength concrete and rock protection structures poses major challenges for projectile penetration projectiles. Increasing the impact velocity of projectiles is an effective way to increase its destructive capability. However, with an increase in the penetration velocity, the warhead is subjected to higher impact loads, which may lead to deformation and damage to the structure, damage to the charge, and seriously affect the combat effectiveness of the warhead (Li, 2021).

Received january 17, 2025. In revised form march 09, 2025. Accepted march 24, 2025. Available online march 25, 2025.
https://doi.org/10.1590/1679-7825/e8546

Studies have been conducted to characterize the dynamic response of warheads and charges. Bi et al. (2022) report that the combined effect of axial and transverse accelerations when the warhead obliquely penetrates a multilayer target causes a crack zone to appear and evolve at an angle to the transverse direction of the charge. Li et al. (2020) highlighted that microcrack interface friction during the penetration process plays an important role in the damage, heating, and localization of PBX1314. Shi et al. (2019) found that increasing the head curvature ratio of the projectile is beneficial to reduce the charge damage. Zhang et al. (2011) found that charge acceleration and length are important factors affecting charge stability. Zhang et al. (2023) and Zhang et al. (2018) simulated the stress wave propagation, pressure distribution, and damage distribution evolution law within the charge.

Numerical simulation technology can intuitively obtain the transient action process of the projectile and target, which is widely used in the study of the penetration problems, and therefore, it is important to adopt a simplified and accurate calculation method (Deng et al, 2016). The numerical calculation method of projectile-target separation replaces the target with the target resistance, which greatly improves computational efficiency. Warren and Tabbara (2000) first realized the simulation process of the projectile penetration into 6016 aluminum targets with different impact angles using the projectile-target separation numerical calculation method on PRONTO 3D. With the projectile-target separation method, based on the cavity expansion model, Kong et al. (2014), He (2007), Fang et al. (2014), Chen et al. (2017) performed the numerical calculations of the projectile obliquely penetrating into concrete target, metal target, and rock target, taking into account the free surface effect. Deng (2018) and Du (2021) analyzed trajectory characteristics based on local interaction theory. In an investigation into the effect of the projectile nose shape on the penetration performance, Yoo et al. (2019) employed the projectile-target separation computational method and discovered a positive correlation between penetration depth and the head curvature-diameter ratio.

In conclusion, extensive research has been conducted on the dynamic response of projectile structures and charges, with a particular focus on low-velocity drop and falling hammer dynamics. These studies also analyzed the results of explosive charge damage. Currently, the dynamic responses of the projectile and charge structure parameters remain unclear with regard to the high-velocity penetration process. The experiments on the response of the projectile structure were conducted using a typical ballistic gun. By combining the numerical calculation method of projectile-target separation, a dynamic response simulation model of the projectile and charge was established. The dynamic response characteristics of a typical projectile and charge structural parameters in the process of encroachment and penetration were analyzed in this study. The findings offer valuable insights for the design of high-velocity impact components and rapid assessment of charge stability.

2 Experiments of projectile penetration into concrete target

The structural response of a projectile can be obtained directly through experiments. Results have shown that the target resistance value during projectile penetration into concrete is directly related to the dynamics of the penetration process. To further study the structural response characteristics, based on a 30-mm short-barreled smoothbore gun, experiments were conducted using projectiles with a diameter of 23.6 mm into a concrete target at impact angles of 0°, 10°, and 20° and velocities ranging from 500 m/s to 900 m/s. A high-speed camera was used to record the attitude and initial velocity of the projectile upon initial impact.

2.1 Experimental Layout

Experiments with projectile penetration into concrete were conducted using a 30-mm ballistic gun. To obtain a high impact velocity, the projectiles were launched using a sub-caliber launching technique. Fig. 1 presents the layout of the experiment. A high-speed camera was employed to capture the projectile flight and targeting attitude. The initial velocity of projectile penetration was calculated by combining the high-speed camera frame rate and the distance of the projectile on the screen; a plane mirror placed at an angle of 45° in front of the target was simultaneously used to record the flight attitude of the projectile.

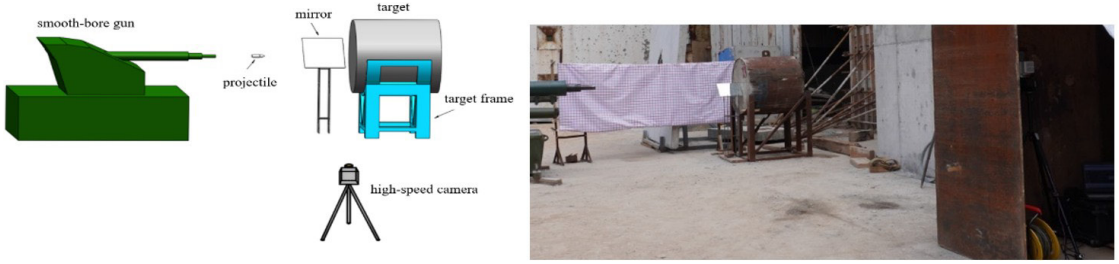

(a) Schematic diagram of the test layout (b) photos of the test layout

Figure 1. Layout of the experiments

2.2 Projectiles and targets for penetration experiments

The projectiles had a diameter of 23.6 mm, a length of 144 mm, and a mass of 367±2 g. To capture the structural deformation characteristics, the projectiles were manufactured using 45 steel, known for its high deformation capacity and excellent mechanical properties. The projectile's structural parameters are detailed in Fig. 2.

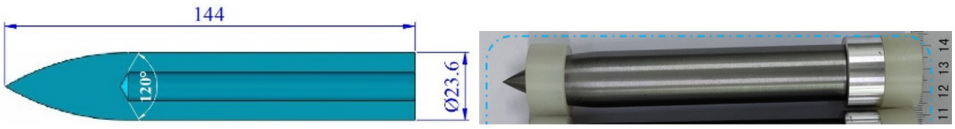

Figure 2. Schematic diagram and photograph of the projectile

As shown in Fig. 2, The projectile used in the experiment is divided into four parts: projectile, sabot, obturator, and sealing device. To reduce the boundary effect on the penetration process in the experiment, the target diameter was selected as 30 times the projectile, which was taken as Φ1000 × 1000 mm for the penetration experiment. A steel cylinder with thickness of 5mm was used to enhance the target restraint, as shown in Fig. 3. Average quasi-static compressive strength of the targets were obtained as 40 MPa.

Figure 3. Concrete target

2.3 Experimental results

During penetration process, the impact attitude of the projectile represents a significant variable for the analysis of the penetration process. The attitude of the projectile was observed and recorded with the high-speed camera. Typical photographs are presented in Fig. 4. As can be seen in the images, the projectile impacted the target surface in the central region. The crater and tunnel parameters of the concrete target were obtained, the concrete target was dissected, and the residual projectile was recovered.

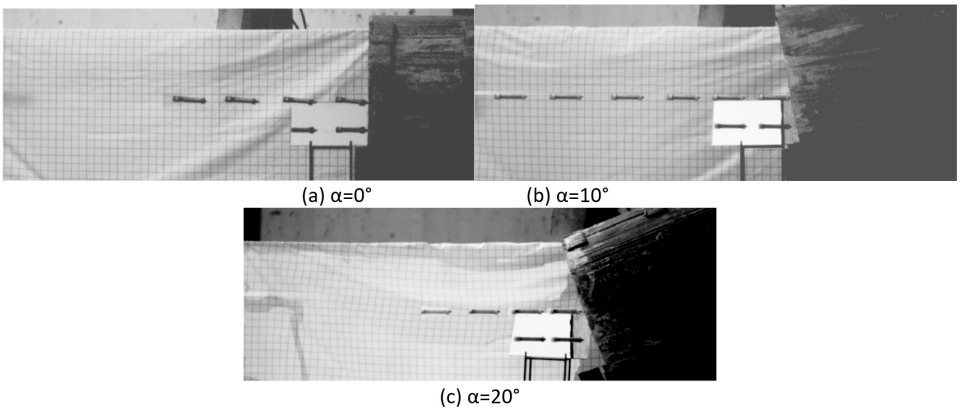

(a) α=0° (b) α=10°

(c) α=20°

Figure 4. Part of the projectile flight targeting attitude

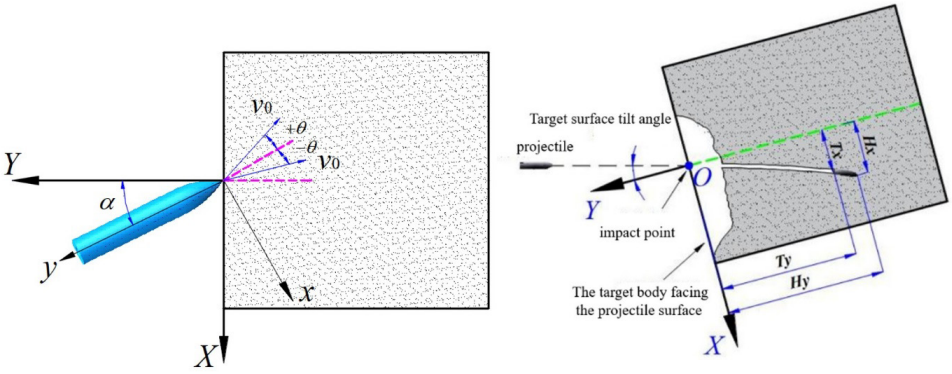

Figure 5. Schematic diagram of the impact attitude of the projectile

To ensure consistency between the initial condition settings of the subsequent simulation calculations and the actual situation, the actual impact angle of the projectile was measured using image processing software. Fig. 4. shows the typical photos of the projectile landing on the target. The *Y*-axis is normal to the surface of the target, v_0 is the initial velocity of the projectile intrusion obtained by the high-speed camera; α is defined as the impact angle of the projectile in the vertical direction, and ϑ is the angle of attack of the projectile in the vertical direction. As illustrated in Fig. 5, it is assumed that the projectile only moves in the *XOY* plane, the origin of the coordinate system, designated as point O, represents the impact point of the projectile. As shown in Fig. 5, the direction perpendicular to the target, which meets the projectile surface, is defined as the Y-axis. The displacement of the projectile in the *Y*-axis direction is the longitudinal displacement; parallel to the target surface as the *X*-axis, the displacement of the projectile in the *X*-axis direction is the transversal displacement, H_x is the transversal displacement of the head of the projectile, and H_y is the longitudinal displacement of the head of the projectile. H_x represents the transverse displacement of the head of the projectile, H_y represents the longitudinal displacement of the head of the projectile, T_x represents the transverse displacement of the tail of the projectile, and T_y represents the longitudinal displacement of the tail of the projectile. The initial impact velocity of the projectile is calculated. The detailed data are shown in Table 1.

(a) α=5.96° (b) α=9.42° (c) α=20°

Figure 6. Typical photos of target dissection

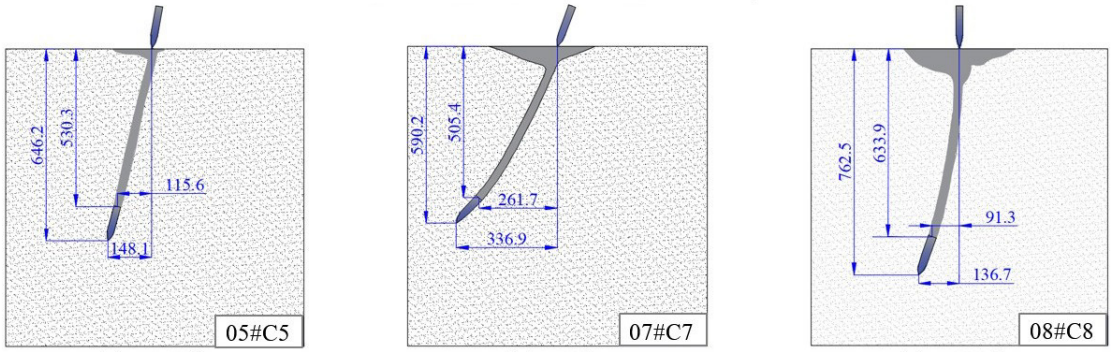

(a) α=9.75° (b) α=20° (c) α=0.58°

Figure 7. Typical trajectory of the projectile

After the experiment, a quick-setting epoxy resin was poured into the target, and after the epoxy resin had completely solidified, the concrete target was dissected, as illustrated in Fig. 6. The solidified and molded epoxy resin was removed, and with the help of image processing software, the trajectory of the projectile in the target was

coordinated and the projectile intrusion displacement was measured. Schematics of craters and tunnels with typical impact velocities are illustrated in Fig. 7, The parameters for the crater and tunnel are listed in Table 1.

Table 1 Penetration experimental results

No.	projectile	v_0/m·s^{-1}	α/°	ϑ/°	H_x/mm	H_y/mm	T_x/mm	T_y/mm
1	C1	516.8	5.96	0.46	58.7	281.8	29.0	155.3
2	C2	561.0	0.40	0.0	3.52	314.4	1.92	170.3
3	C3	584.3	10.5	0.10	81.4	349.6	47.2	212.0
4	C4	708.0	9.42	0.45	90.5	448.2	60.6	313.7
5	C5	827.5	9.75	0.0	148.1	646.2	115.6	529.8
6	C6	594.7	20.0	1.23	154.9	316.0	91.5	202.1
7	C7	820.1	20.0	0.10	336.9	590.2	261.8	505.4
8	C8	893.0	0.58	0.0				

2.3.1 Damage to Targets

Fig.8 illustrates the typical moments of destruction of the target during the penetration process. As shown in Fig. 8, the impact point was stripped near the concrete medium. This phenomenon, which occurs at a specific angle, is attributed to the impact of the projectile on the target body, which generates a strong compression wave that rapidly propagates toward the target. Subsequent to the reflection of the formation of tensile waves, the coupling effect of the tensile wave and projectile shear extrusion gives rise to stripping and splashing of the concrete media. As penetration progressed, a significant number of cracks emerge on the surface of concrete. The free surface of the target and the residual tensile wave exert a combined effect, resulting in a perceptible bulging phenomenon on the target surface. Peeling and splashing of the concrete medium gradually increases in tandem with this process.

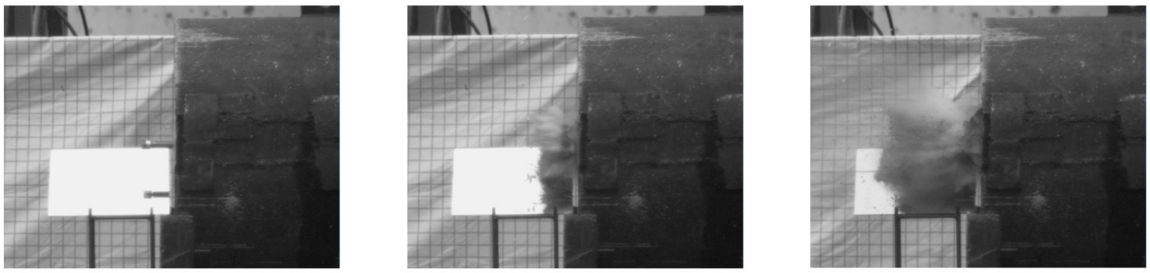

Figure 8. Process of formation of open pit area

The crater areas on the surface of the target were identified using 3D scanning imaging equipment. The selection of these scans is presented in Fig.9. Fig. 9 illustrates a notable discrepancy in the volume of craters on the upper and lower sides of the tunnel area borehole during oblique intrusion. Conversely, during positive intrusion, the destruction of the target surface exhibits a circular shape, forming a predominantly symmetrical crater area in relation to the point of impingement.

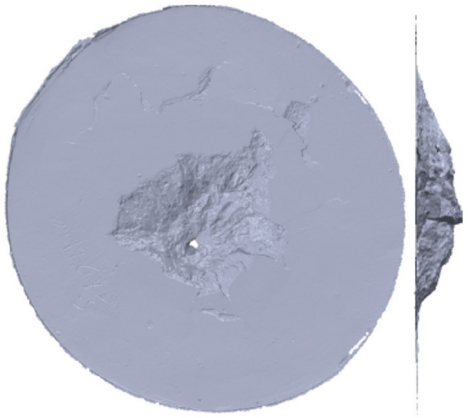

Figure 9. Partial Scanning Results

The crater depth on the target surface are shown in Fig. 10. Cratering parameters have been investigated for projectiles penetrating different concrete targets, and different prediction models have been given for the cratering depths. The depth of the cratered area is usually expressed as k times the diameter of the projectile. According to the crater depth prediction model, the coefficient of craters depth are written as a linear relationship with $m^{0.5}v_0^{0.5}$, v_0, v_0^c, H/d, where m is the mass of the projectile, v_0 is the impact volcity and c is a constant, H is penetration deep of the target. According to the predictive model, the depth of the craters are obtained. Which are given in the Fig. 10. According to the test results, it is obtained that the depth of the crater is basically within the range of 2~2.5 times of the projectile diameter. Based on the test results of the average crater depth, the average value of crater depth k = 2.37 is obtained.

The post-processing software Geomagic Wrap was employed to calculate the crater parameter. The results are presented in Fig. 10 and Fig. 11. It is found that the volume of the crater shows an increasing trend with the increase of the projectile impact angle.

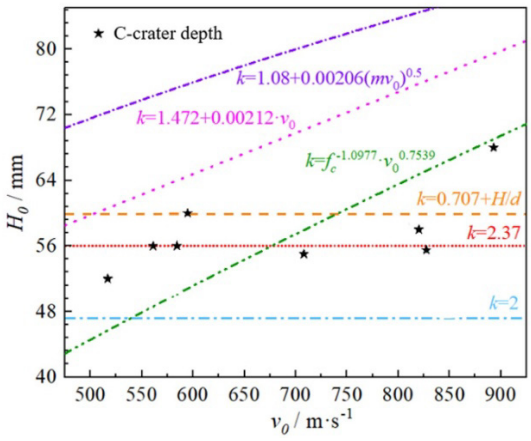

Figure 10. Depth of the crater

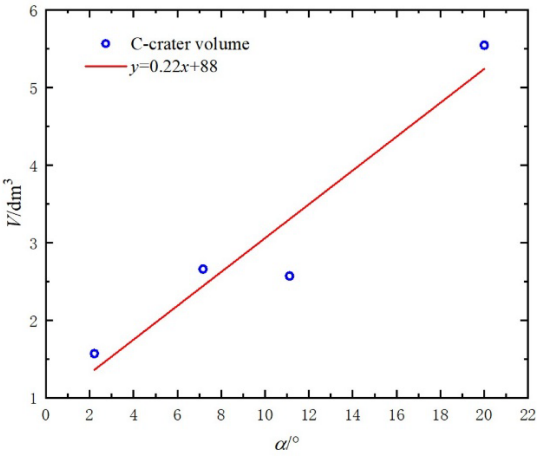

Figure 11. Volume of the crater

2.3.2 Deformation of the residual projectile

As a consequence of the extrusion and friction between the projectile and the target during the penetration process, a layer of concrete powder is deposited on the surface of the projectile when the target is subsequently dismantled. Fig.12 illustrates the morphology of the projectile following the removal of the concrete powder from the surface. It can be observed that the projectile body remains intact. However, the projectile exhibits a darker colouration and a greater number of discernible scratches on the surface, indicative of significant friction between the target and the projectile during penetration. When the initial velocity of penetration is high, the stress wave inside the projectile may exceed the yield strength limit of the material, resulting in significant deformation. Concurrently, the thermal softening of the material is more pronounced. It can be seen from Fig. 12 that mass erosion is an inevitable consequence of high-velocity penetration. This phenomenon is most pronounced in the nose of the projectile. The presence of mass loss gives rise to more pronounced asymmetric forces acting on the projectile during the penetration process.

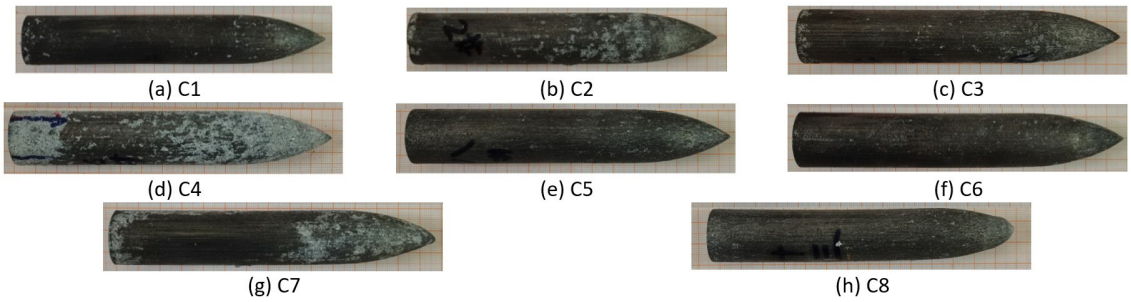

Figure 12 Picture of residual projectile

In order to provide a more detailed quantitative analysis of the damage in the projectile, Fig.13 present a summary of the damage response of the projectile with different initial velocity and angles. Fig.13 illustrates that as the initial velocity of penetration increases, the mass loss rate of the projectile rises, though it remains below 4.5%. The length shortening rate of the projectile is approximately 6%, with a non-linear increase in velocity. This indicates that the shortening of the projectile's length is influenced by not only the penetration velocity but also the impact angle.

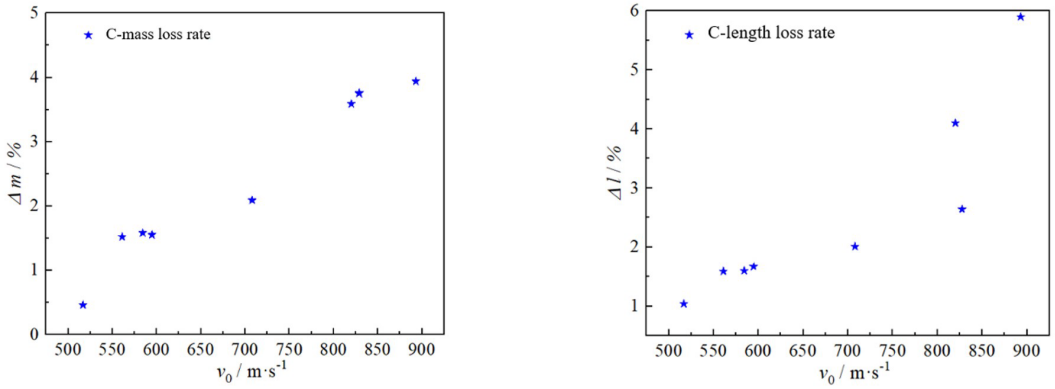

(a) Mass loss as a function of velocity (b) Length loss as a function of velocity

Figure 13. Mass, length loss of projectiles

3 Analysis of the dynamic response of projectiles penetration into a semi-infinite concrete target

3.1 Penetration resistance

Based on the cratering effect of the projectile penetrating obliquely into the concrete target, the splash streamline field of the cratering stage were analyzed. The penetration resistance during the cratering stage was modified by taking the the energy conservation equations of the splash streamline into account.

Volume of streamline during the penetration process is considered as a sector region with a height of Δ*z* and a length of Le. Equation of the streamline volume during penetration is:

$$V_{\text{tube}} = [(L_{\text{e}} + \rho)^2 - \rho^2]\Delta\theta\Delta z = (2\rho L_{\text{e}} + L_{\text{e}}^2)\Delta\theta\Delta z \tag{1}$$

where ρ is the polar radius, Δϑ is the radius angle of the projectile surface element, Δ*z* is the length of the projectile axis corresponding to the projectile surface element.

The splashing streamline strength energy(Li P C et al, 2024) during penetration was obtained:

$$E_{\text{strength}} = \varepsilon\sigma_{\text{cf}}(2\rho L_{\text{e}} + L_{\text{e}}^2)\Delta\theta\Delta z \tag{2}$$

where ε is the volumetric strain, σcf is the uniaxial compressive strength.

Based on the assumption that kinetic energy of the input streamline and the medium between the surface of the projectile and the wave front are the same. Therefore, the kinetic energiesC of the input streamline is:

$$E_{\text{kin}} = \frac{1}{2} Q_1 \left(\int_0^l (\mathrm{R} + w)(\rho + w \sin \varphi)(v_w)^2 d\, w \right) \mathrm{d}S / \mathrm{R}\rho \tag{3}$$

where Q_1 is limit density (the density of the complete collapse state of the pores in the concrete), l is the distance from the wave front to the surface of the projectile (Li P C et al, 2023), dS is the area of the surface elements of the projectile, w is the distance from the normal compression medium to the surface of the projectile, v_{w} is velocity of normal moving medium at different positions.

The residual kinetic energy of streamline is obtained

$$E_{\text{re}} = E_{\text{kin}} - E_{\text{strength}} \tag{4}$$

Therefore, the stress of the projectile surface during the cratering stage is obtained

$$\sigma_n = \begin{cases} 0 \; E_{\text{re}} \geq 0 \\ \sigma_{\text{r}} \; E_{\text{re}} < 0 \end{cases} \tag{5}$$

where σ_r is the radial stress at cavity surface.

According to the analysis of the projectile penetration process, when the angle ϕ between the target and the nose of the projectile is less than the minimum separation angle ϕ_{min}, the stress of target acting on the projectile surface element will be zero, otherwise, the stress will equal to the radial stress at cavity surface.

$$\sigma_n = \begin{cases} \sigma_{\text{r}} \;\; \phi > \phi_{\min} \\ 0 \;\;\; \phi \leq \phi_{\min} \end{cases} \tag{6}$$

The target resistance exerts a direct influence on the penetration action of the projectile. Based on the target material incompressibility assumption, Warren and Forquin (2016) proposed a quasi-static stress expression for the expanding surface of the spherical cavity in plastically cracked elastic material (Forrestal and Longcope, 1990). that is:

$$\sigma_r = \frac{Y}{\lambda} \left[\frac{2}{\alpha} \left(\frac{c}{a} \right)^{\alpha\lambda} - \left(\frac{3-\lambda}{3} \right) \right] \tag{7}$$

$$\left(\frac{a}{c} \right)^3 = \frac{9Y}{4E} \left(\frac{Y}{2T} \right)^{\frac{1}{2}} \tag{8}$$

Where: α=6/(3+2λ), Y is the uniaxial compressive strength of the target, λ is the pressure hardening coefficient of the target,E is the elastic modulus of the target, T is the tensile strength of the target, and σ_r is the quasi-static radial stress.

Then the dynamic resistance during crater stange can be obtainde by Eq(1)-(4), dynamic resistance during tunnel stange can be obtainde by Eq(9).

$$\sigma_n = \frac{Y}{\lambda} \left[\frac{2}{\alpha} \left(\frac{c}{a} \right)^{\alpha\lambda} - \left(\frac{3-\lambda}{3} \right) \right] + \rho_0 \cdot v_n^2 \, H_1 \geq kD \tag{9}$$

Where: ρ_0 is the target density, v_{n} is the surface normal velocity of the spherical cavity, y is the depth of the pitted area,k is the coefficient of pitted depth, and D is the diameter of the projectile.

3.2 Simulation method of projectile-target separation

To reduce the influence of the target boundary effect on the penetration performance, size of the target will be set relatively large, generally more than 30 times the size of the projectile. However, The utilisation of a full simulation including projectile and target for the execution of pertinent calculations and analyses invariably results in a marked reduction in operational efficiency and an attendant diminution in processing speed. Concurrently, the failure and mesh deletion of the target in the simulation will precipitate a sudden change in the force between the projectile and target interface, which will be an great effect on the structural response of the projectile. Combined with the free surface and crater resistance attenuation effect, target resistance model are formed. The application of target resistance to the projectile ensures that the influence of sudden changes in resistance on structural response will be effectively mitigated.

Simultaneously, the calculation of numerous meshes is circumvented and the computational efficiency is enhanced. Consequently, the projectile-target separation calculation method exhibits a great advantage in characterising the structural response of the projectile.

In simulations of the projectile-target separation method, the target action is substituted with the resistance exhibited by the projectile surface unit. Figure 1 illustrates a schematic representation of the forces acting on the surface unit of the projectile within the target, with the target resistance applied to the nodes of the surface unit of the projectile.

Parameters of the oblique penetration process of the projectile are calculated, and the spatial coordinates and normal velocities of all the nodes on the surface of the projectile are extracted by the subroutine within each time step.The surface nodes of the projectile are then judged as to whether they are inside the target or not by the boundary conditions of the target that have been set in the subroutine. In the event that the surface nodes of the projectile body are found to be within the target, the normal velocity of the nodes is incorporated into the target resistance function for calculation. If the final calculation of the resistance of the nodes is found to be non-zero, it can be deduced that the nodes are in contact with the target, and consequently, all the nodes in contact with the target constitute a surface for the projectile-target contact surface. As the penetration process continues, an increasing number of nodes will cross the target boundary, resulting in a modification of the number of nodes in contact with the target body and, consequently, a gradual alteration in the contact surface of theprojectile and target.

The normal stress at each node can be determined from Fig.14 as:

$$\sigma_n = \frac{Y}{\lambda}\left[\frac{2}{\alpha}\left(\frac{c}{a}\right)^{\alpha\lambda} - \left(\frac{3-\lambda}{3}\right)\right] + \rho_0 \cdot (\boldsymbol{v}_k \cdot \boldsymbol{n})^2 H_1 \geq kD \tag{10}$$

where v_k is the velocity vector at node *k* and *n* is the direction normal to the outside of the node of the elastomer surface unit. The resistance function assumed by He (2007) is used to ensure the continuity of the normal stress on the contact surface of the projectile target in this region. As shown in Eq. (3), the drag force on the projectile varies with v_k and *n* during the encroachment process, and the drag force starts to appear only when the surface unit of the projectile enters within the target boundary conditions; conversely, when the surface unit of the projectile is located outside of the target boundary conditions, the projectile is not subjected to a force (Deng, 2018).

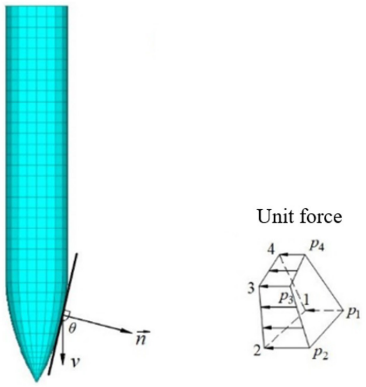

Figure 14. Diagram of projectile surface pressure.

3.3 Numerical simulation of projectile penetration into concrete targets

3.3.1 Model of projectile penetrating a semi-infinite concrete target

The Johnson-Cook model is widely used in simulation calculations to describe the deformation behavior of metallic materials under large deformation and high strain rate conditions. The structure of the model is relatively simple, and integrates the effects of strain hardening, strain-rate strengthening, and temperature softening, which are expressed as follows:

$$\sigma = \left(A + B\bar{\varepsilon}_p^n\right)\left(1 + C\ln\bar{\varepsilon}^*\right)\left(1 - \frac{T - T_{room}}{T_{melt} - T_{room}}\right)^m \tag{11}$$

where σ is the flow yield stress. *A* is the initial yield stress at the reference strain rate and reference temperature; *B* is the hardening modulus of the metallic material; *n* is the dimensionless hardening exponent of the material. It can be

seen that the plastic flow direction of the material is related to the value of *n*. *C* and *m* are dimensionless parameters, which are the strain rate strengthening coefficient and temperature softening index, respectively. T_{room} is the ambient temperature, which is usually assumed as 294K, while T_{melt} is the melting temperature of the material, and *T* is the current moment temperature of the material. The values of *A*, *B,* and *n* can be obtained by fitting the stress-strain curves of the tensile test, and the method of obtaining them is relatively simple, so the Johnson-Cook intrinsic model is widely used in numerical simulation calculations in the field of impact dynamics.

To gain further insight into the deformation of the projectile due to the asymmetric force during the penetration process, the Johnson-Cook model is used in the simulation. The parameters are listed in Table 2.

Table 2 Parameters of Projectile (Ng et al, 2002)

***A*/MPa**	***B*/MPa**	***C***	***m***	***n***	***Tm*/K**
950	725	0.015	0.625	0.375	1765

The target body was a semi-infinite concrete target with an unconfined compressive strength of 40 MPa. Its main parameters are listed in Table 3.

Table 3 Concrete target material parameters (Li et al, 2009)

ρ_t / g·cm^{-3}	f_t / MPa	*E* / *GPa*	τ / MPa	λ
2.4	40	32.5	31.07	0.67

The Lagrangian algorithm was used to describe the dynamic deformation and damage behavior of the projectile, with an average mesh size of 1.2 mm × 1.2 mm × 1.2 mm, and the whole projectile is divided into 59200 meshes with a total of 64967 nodes. During the experiments, the impact angle and initial velocity of the projectile were obtained through high-speed camera, and it was found that there was a slight deviation between the actual impact angle and the target angle. The initial condition were set up in the ABAQUS pre-processing module to make them consistent with the actual penetration conditions. In addition, according to the projectile-target separation calculation, the targeting point is set as the origin of the coordinate system, the *y* = 0 plane is set as the projectile target meeting surface, and the negative direction of the *y*-axis is set as the direction of the projectile's penetration.

3.3.2 Numerical simulation results and analysis of projectile penetration into semi-infinite concrete target

Detailed comparisons of the nose and tail of the projectile with the experimental data in the results of the numerical simulation of the projectile -target separation are given in Fig. 15 and Fig. 16. As shown in Fig. 15, the numerical simulation results are in good agreement with the experimental data, and the maximum error is less than 6%. With the increase of the penetration velocity, the displacement of the projectile in both the direction perpendicular to the target surface and the direction parallel to the target surface shows an increasing trend.

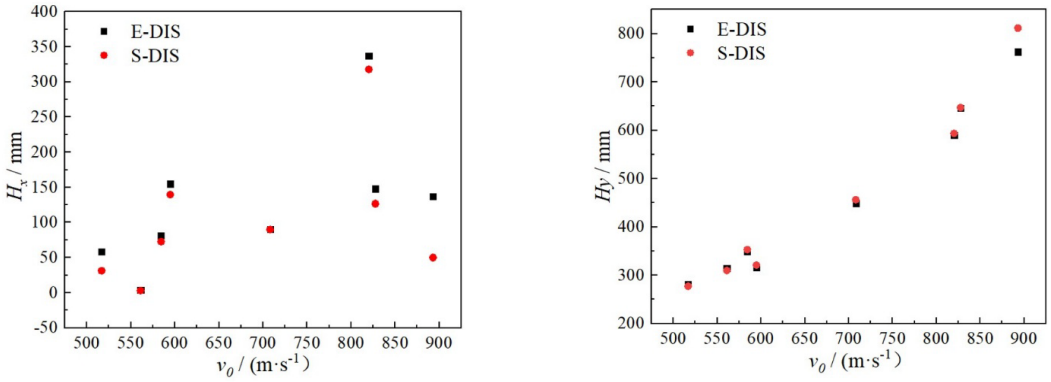

(a) Comparison of transverse displacements (b) Comparison of longitudinal displacements

Figure 15 Results of simulation and experiment for displacement of the nose of the projectile

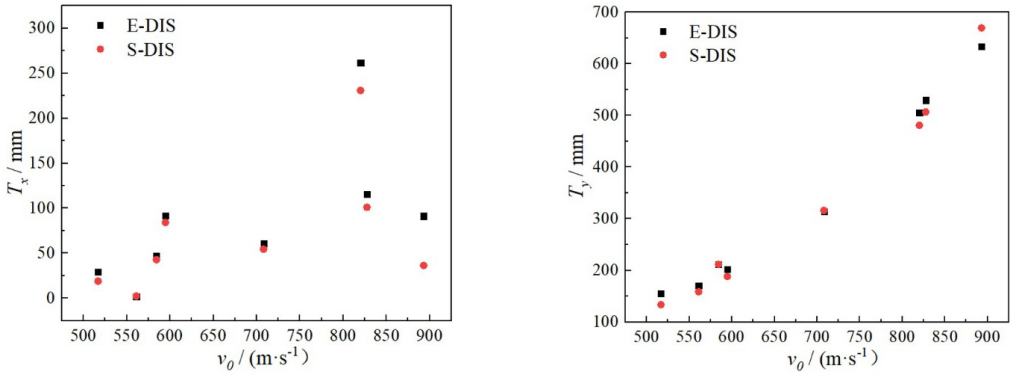

(a) Comparison of transverse displacements (b) Comparison of longitudinal displacements

Figure 16 Comparison between simulation and test for displacement of the tail of the projectile

Fig. 16 illustrates the equivalent plastic deformation of the final moment of the remaining elastomer cloud diagram and the test of the recovered elastomer pair ratio. It is observed that the elastomer exhibits different degrees of plastic deformation, which is due to the the role of the asymmetric force is to create an uneven distribution of the elastomer surface on both the upper and lower sides of the plastic deformation. This inhomogeneous deformation causes deformation of the projectile. Furthermore, the high pressure on the nose of the projectile renders it susceptible to damage during penetration. This is evidenced by the maximum equivalent plastic strain occurring at the projectile nose, as shown in Fig. 17.

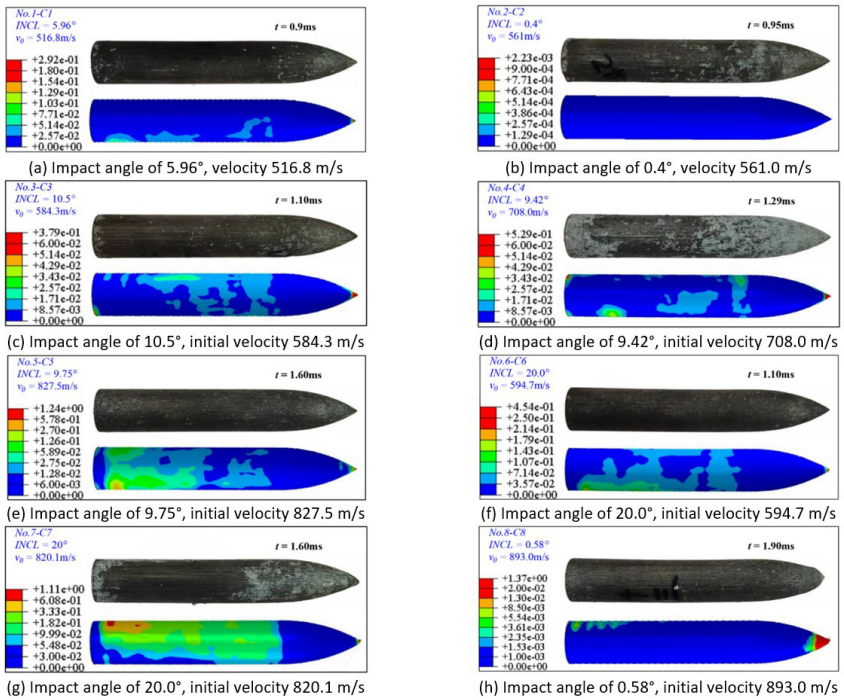

(a) Impact angle of 5.96°, velocity 516.8 m/s (b) Impact angle of 0.4°, velocity 561.0 m/s

(c) Impact angle of 10.5°, initial velocity 584.3 m/s (d) Impact angle of 9.42°, initial velocity 708.0 m/s

(e) Impact angle of 9.75°, initial velocity 827.5 m/s (f) Impact angle of 20.0°, initial velocity 594.7 m/s

(g) Impact angle of 20.0°, initial velocity 820.1 m/s (h) Impact angle of 0.58°, initial velocity 893.0 m/s

Figure 17 Comparison of projectile deformation between simulation and experiment

Concurrently, the interaction between the projectile tail and the target medium persists throughout the penetration process, thereby facilitating substantial plastic deformation in the vicinity of the projectile tail. The penetration velocity exerts an influencesd on the inertial term of the target drag during the penetration process, whereas the targeting angle exerts an influencesd on the asymmetric loading effect during the penetration process. Both of of these factors contribute to an increaseaugmentation in the degree of plastic deformation and damage to the projectile.

The trajectories of the projectile in the numerical simulation calculations are extracted and compared with the experimental penetration trajectories, as illustrated in Fig. 18. A comparison of the two results reveals a high degree of agreement, which further indicates that the numerical simulation method of projectile-target separation adopted in this paper can accurately reflect the force and motion state of the projectile within the target.

As shown in Fig. 18, the projectile exhibits a linear trajectory into the concrete target when the initial velocity of the projectile is under 800 m/s. The projectile did not exhibit any obvious attitude deflection during the intrusion process, as

observed in Figs. 18(b)–(d) and 18 (f). For C1 projectile in Fig. 18(a), the presence of the angle of attack at the time of the target landing causes the trajectory to appear deflected, even when the projectile intrudes at a low velocity. While the trajectory is relatively straight in the initial stage when the initial velocity is high, as the intrusion continued, the projectile structure exhibits different degrees of deformation under the action of the forces on the target, resulting in an obvious deflection of the trajectory during the penetration process, as shown in Figs. 18(g) and 18(h). The combination of experimental and numerical simulation results demonstrates that mass abrasion at the nose of a projectile with high velocities and the asymmetric force under oblique penetration are the main factors influencing ballistic instability.

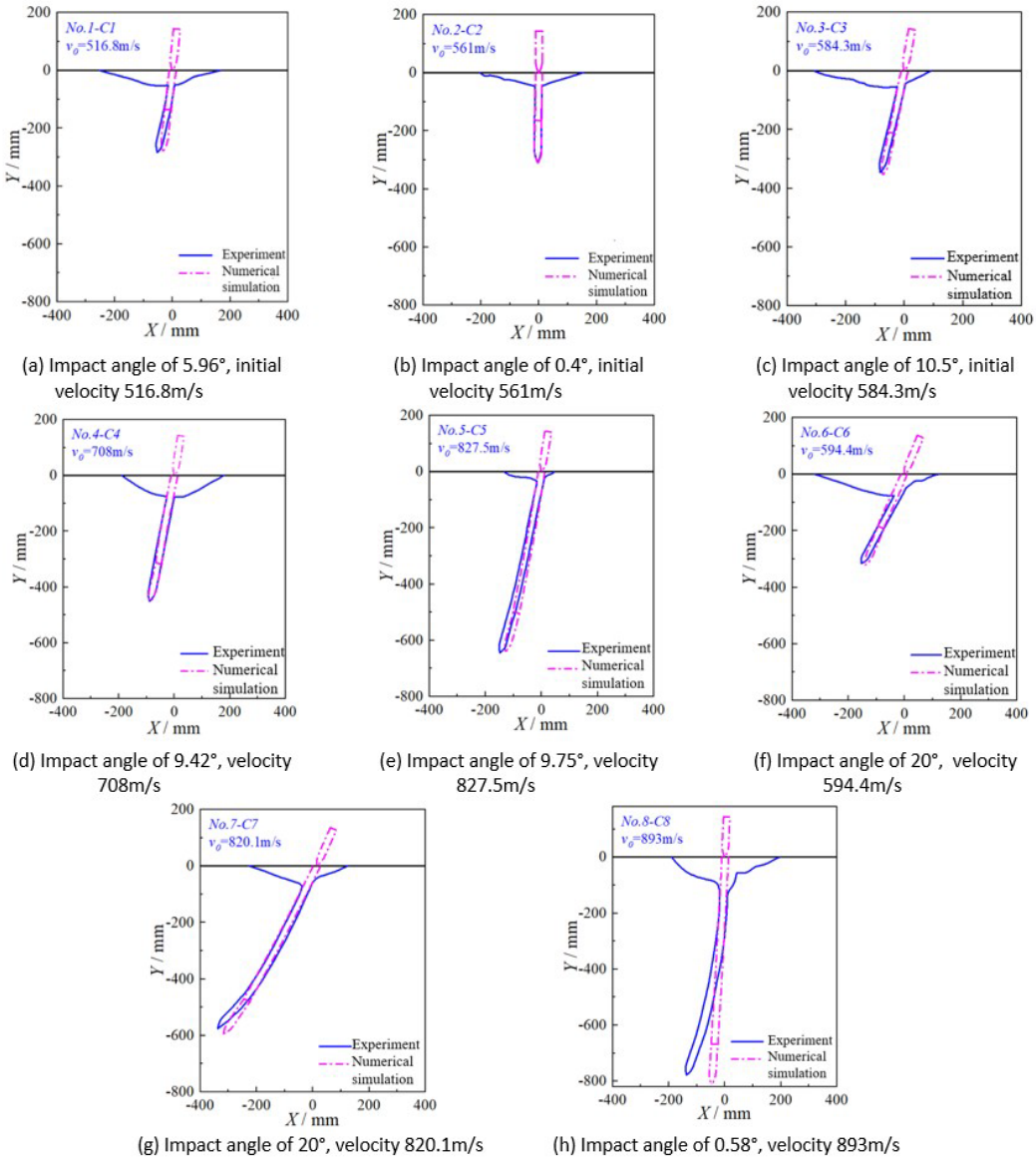

(a) Impact angle of 5.96°, initial velocity 516.8m/s

(b) Impact angle of 0.4°, initial velocity 561m/s

(c) Impact angle of 10.5°, initial velocity 584.3m/s

(d) Impact angle of 9.42°, velocity 708m/s

(e) Impact angle of 9.75°, velocity 827.5m/s

(f) Impact angle of 20°, velocity 594.4m/s

(g) Impact angle of 20°, velocity 820.1m/s

(h) Impact angle of 0.58°, velocity 893m/s

Figure 18 Comparison of projectile penetration ballistics

During positive penetration, a compression wave is generated at the projectile's nose upon initial contact with the target surface and propagates toward the projectile's tail. The propagation this stress wave can be directly observed through numerical simulations. Fig. 19 plots the axial stress distribution of the projectile at various penetration intervals.

When obliquely intruded, the stresses on the projectile surface no longer exhibit a uniform distribution. This variation arises from differences in the direction of the normal velocity of the microelements on the surface of the projectile and the distance from the microelements to the free surface. Fig. 20 plots the equivalent plastic strain evolution of the projectile during penetration. As observed, the projectile forms a compression wave in the head after colliding with the target, which propagates to the projectile. The stress amplitude at the time of hitting the target was only 45 MPa because of the weakening effect of the crater and free-surface effects on the resistance of the target. As the intrusion proceeded, the stresses were mainly concentrated in the region of the projectile wall thickness mutation, as

illustrated in Fig. 20(c). Subsequently, the compression wave is reflected to form a tensile wave, and under the superposition of the tensile and compression waves, the stress amplitude on the projectile is always greater than the yield strength of the projectile.

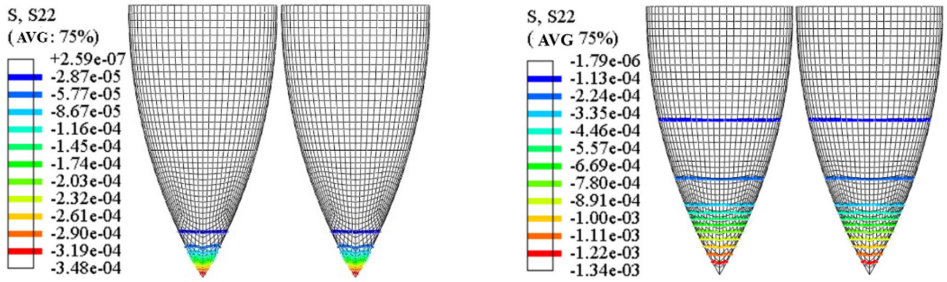

(a) t =6.4 μs (b) t =20 μs

Figure 19 Axial stress map

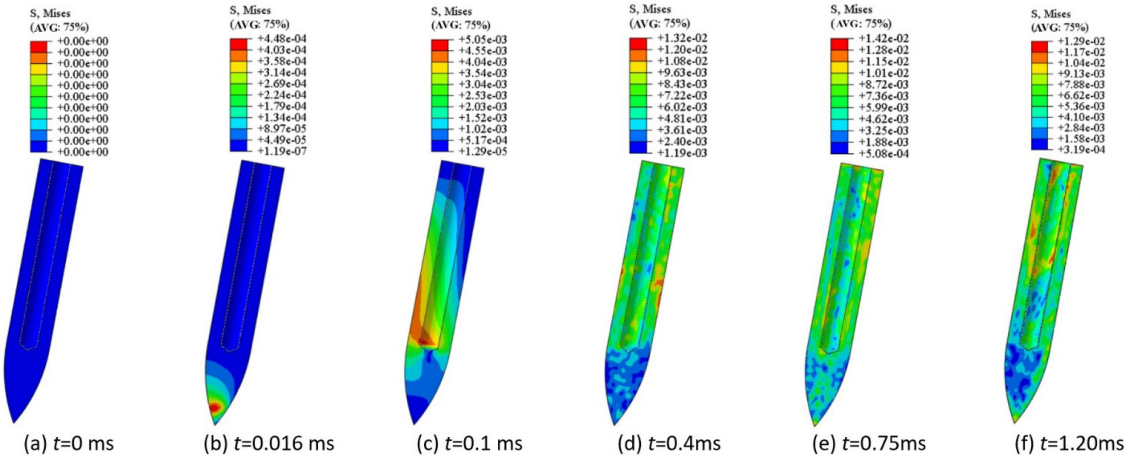

(a) t=0 ms (b) t=0.016 ms (c) t=0.1 ms (d) t=0.4ms (e) t=0.75ms (f) t=1.20ms

Figure 20 Map for projectile von-mises stress with impact velocity of 584.3m/s

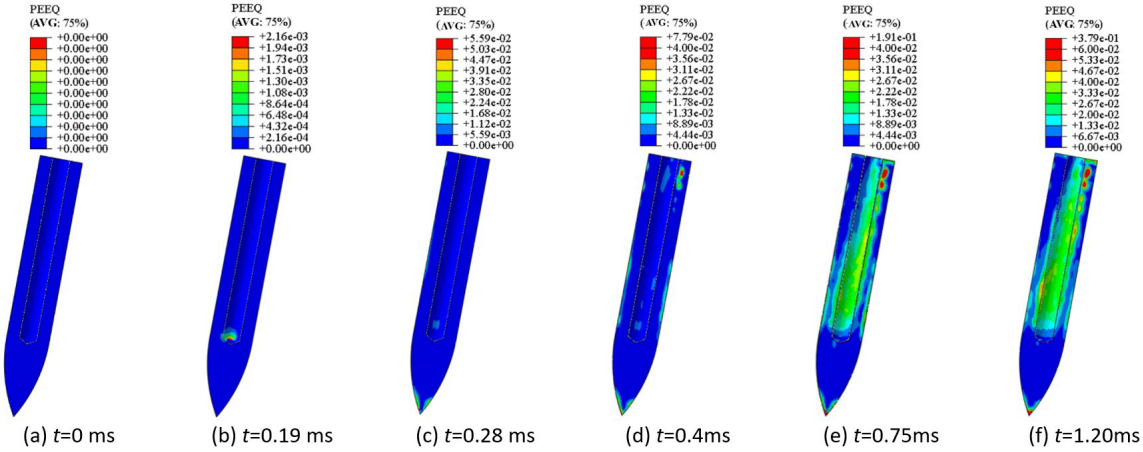

(a) t=0 ms (b) t=0.19 ms (c) t=0.28 ms (d) t=0.4ms (e) t=0.75ms (f) t=1.20ms

Figure 21 Map of equivalent strain for projectile with impact velocity of 584.3m/s

Fig. 21 presents the distribution of equivalent plastic strain in the C3 projectile during the intrusion process; no plastic deformation is evident in the projectile before 0.19 ms. At the moment of 0.19 ms, a plastic strain with an amplitude of 0.022 occurs with a sudden change in the dimensions of the internal cavity of the projectile, as illustrated in Fig. 21(b). As the penetration process progresses, the damage to the projectile nose increases. The continuous action of the asymmetric load and free surface results in the expansion of the distribution area of the plastic strain on the projectile, accompanied by a gradual increase in strain amplitude, as shown in Fig. 21, and the equivalent plastic strain on the projectile shows a clear asymmetric distribution, and the maximum equivalent plastic strain is 0.38 at the nose of

the projectile at t = 1.2 ms. The maximum equivalent plastic strain on the projectile at ms is 0.38, which is located at the nose.

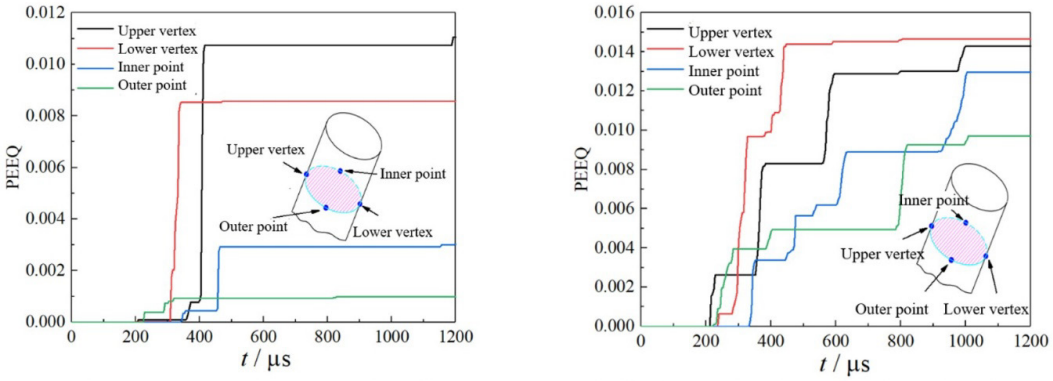

(a) Unit strain in 1/3 projectile length section (b) Unit strain in 1/2 projectile length section

Figure 22 Unit strains on cross sections at different locations

Fig.22 gives the strain time curves of 4 cells in the cross-section at 1/3 and 1/2 of the projectile length from the nose of the projectile, which is located at the upper, lower, and two lateral vertices of the cross-section, respectively. As illustrated in the figure, the two side vertex cells are situated in the neutral plane of the projectile bending. Therefore, the strains on these two cells are lower than the cell strains at the upper and lower vertices of the cross-section, indicating that the bending response of the projectile under oblique intrusion conditions is mainly dominated in the direction along the elastic axis. After approximately 0.2 ms, significant plastic strain becomes evident at the 1/3 length cross-section from the projectile nose. The plastic strain exhibits a “step-like” increase, where the flat segments of the strain curve represent the unloading phase.

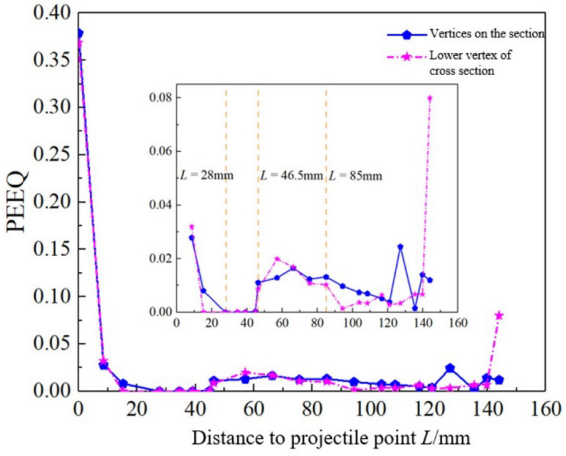

Figure 23 Strain distribution along the axial direction of the projectile

To further quantify the extent of damage to different regions of the projectile, the distribution of the maximum equivalent strain in the surface cell of the projectile along the direction of the projectile axis was determined, as illustrated in Fig. 23. The cross-section of the projectile exhibiting the highest equivalent strain amplitude, with the exception of the head region, occurs in the region between 0.32 and 0.59 times the projectile length, situated at a distance of approximately 46.5 to 85 mm from the projectile nose. In addition, a collision is observed between the tail of the projectile and the concrete target during the oblique penetration process; resulting in a sudden increase in the equivalent plastic strain at the tail of the projectile at a distance of 127.2 mm to 144 mm from the nose (0.88–1.0 times the length of the projectile), with a maximum magnitude of 0.08. The numerical simulation results of the projectile-target separation indicate three main hazardous positions in the oblique penetration process: The first is located at the nose of the projectile, which undergoes significant deformation due to compression waves. The second is located between 0.32 and 0.59 times of the projectile length from the nose, which is mainly affected by compression and tension waves; the third is located in the region of 0.88 to 1.0 times the projectile length from the end of the projectile, which is mainly

characterized by transverse deformation. Thus, these three regions should be prioritized in the projectile design to enhance durability under penetration conditions.

The degree of projectile deformation depends on the initial impact velocity. As the kinetic energy of the projectile increases, the degree of deformation also increases. Fig. 24 presents the equivalent strain at different velocities and angles of projectiles C3, C4, and C5. At comparable targeting angles, an increase in the initial penetration velocity elevates the equivalent strain amplitude at the head and tail of the C4 and C5 projectiles compared to the C3 projectile. However, there is a minimal difference in strain amplitude across the three velocities in the region between 0.32 and 0.59 times the projectile's length from the nose.

To further analyze the relationship between the impact angle and projectile damage, the distribution of equivalent strain at different locations of projectiles C2, C3, and C6 is presented in Fig. 25. For the C2 projectile, which can be considered as undergoing vertical intrusion, the equivalent strain increases closer to the nose, reaching a maximum strain of 0.002 at the tip. However, the overall level of equivalent strain variation in the C2 projectile is lower than that observed for the other two impact angles. As the projectile impact angle increases, the strain amplitude varies significantly in the region from 0.32 to 0.59 times the projectile length from the nose. Therefore, while the initial penetration velocity mainly affects the damage at the nose and tail of the projectile, the impact angle mainly affects the bending deformation of the projectile.

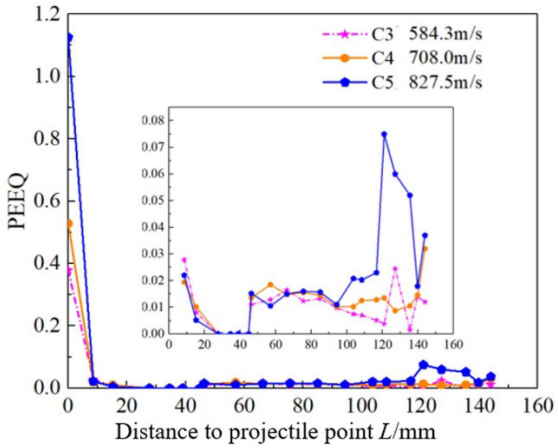

Figure 24 Axial strain distribution of projectile versus impact velocity

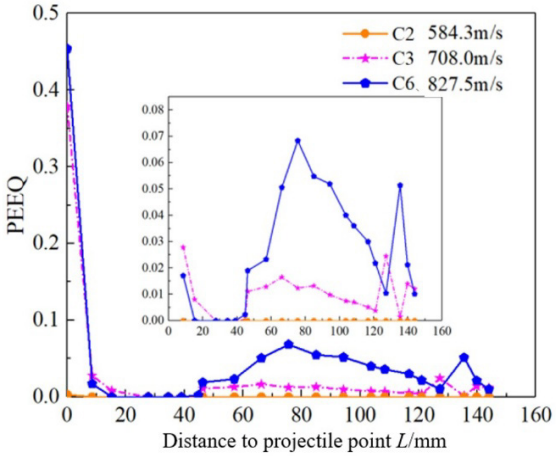

Figure 25 Relationship between axial strain distribution of projectile and impact angle

3.4 Damage response of projectile penetration concrete target

The positive penetration of a charged projectile into a semi-infinite concrete target was calculated. The external geometry of the projectile was identical to that used in the experimental study. Because this study focused only on the stresses on the projectile and charge, the projectile and bottom were regarded as a single entity. The model was simplified into two components: the projectile and charge. Initially, the charge filled the interior of the projectile, and the warhead was modeled as depicted in Fig. 26. The charged material is characterized using a bilinear plastic hardening model with specific material parameters, as listed in Table 4:

Table 4 Charging material parameters (Li, 2021)

ρ / g·cm^{-3}	E / GPa	v	σ_0 / MPa	E_t / MPa
1.85	10.1	0.3	45	600

The contact and friction between the warhead shell and charge, were modeled by assigning a friction coefficient of 0.1 (Li, 2021). The initial impact velocity of the warhead was set to 800 m/s as it penetrated the semi-infinite concrete target with a compressive strength of 40 Mpa. Fig. 27 illustrates the acceleration curves of the warhead shell and charge, which exhibit oscillations around the shell acceleration curve. While the rigid accelerations of the projectile and charge remain consistent, the relative motion between the charge and projectile introduces differences in their structural vibration response. The relative motion acceleration of the charge is $(1\text{-}R_c^{2n}) \cdot Z^*$ times the acceleration of the projectile(Xu et al, 2011), where R_c is the reflection coefficient of the stress wave, n is the number of reflections, and Z^* is the wave impedance ratio. Thus the degree of acceleration curve oscillation is greater for loads with lower material wave impedance and quality. Multiple peaks are observed for both charge and projectile accelerations, and the peaks and valleys of charge accelerations correspond to the valleys of shell accelerations, with the maximum acceleration occurring in the shell near the start position of the tunnel area with a magnitude of 26,965 g, followed by the charge reaching its maximum value of 42,668 g. The maximum acceleration is observed at the start of the tunnel area. In addition, owing to the low modulus of elasticity of the charged material, there is a reverse increase in charge acceleration towards the end of penetration.

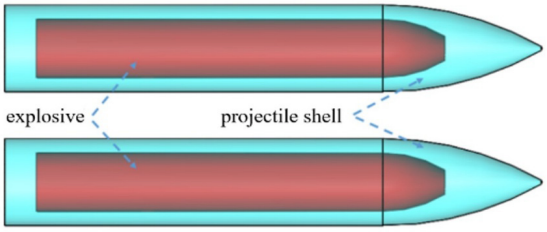

Figure 26 Circular section projectile (shell b/a = 1.0)

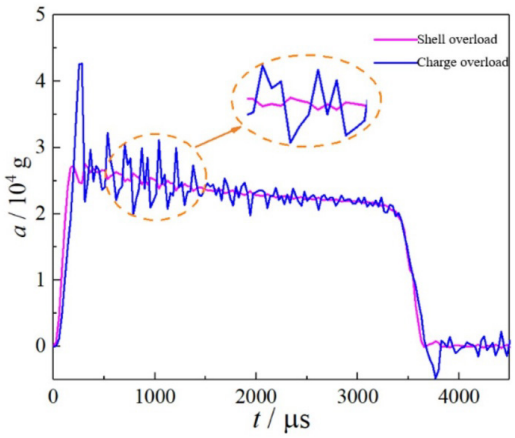

Figure 27 Projectiles and charge accelerations

Figs. 28 and 29, respectively, plot the stress maps of the projectile and charge in the *xoy* and *yoz* profiles. Upon impact of the warhead with the target, the curvature of the projectile's head creates a high-stress region near the central axis of the projectile's nose. Simultaneously, a stress wave propagates rapidly to the aft part of the projectile shell, reaching an amplitude of 246 MPa, as shown in Fig. 28(b). Under the action of the inertial force and stress wave transmitted to the interior of the shell, the stress at the nose of the charge increases rapidly. However, owing to the different material properties of the projectile and charge, the propagation velocity of the stress wave in the projectile is significantly higher than that in the charge. Subsequently, the stress wave continued to propagate toward the end, resulting in several highly stressed annular zones distributed at intervals on the shell, as shown in Figs. 28(c) and (d). At 2.5 ms, two stress concentration zones are formed on the shell, and the maximum equivalent stress on the shell is 763MPa, as shown in Fig. 28(d). At 3.5 ms, the stress amplitude on the projectile decreases to 180 MPa, as plotted in Fig. 28(e). The impact of the

projectile on the target generates a stress wave that transfers into the internal charge. The stress rises in the charged surface and shell contact area, while the curvature of the nose focuses the stress wave along the charge axis, forming a high-stress zone along the charge axis. At this stage, the maximum equivalent stress in the charge reaches 47.2 MPa, exceeding the material's yield strength, as illustrated in Fig. 29(b). As penetration progresses, the superposition of stress waves further increases the stress within the charge, expanding the region of high stress, as illustrated in Fig. 29(c). At 2.5 ms, the residual kinetic energy diminishes, and a tensile wave, reflected from the free surface of the projectile nose, transmits into the internal charge. Although the stress amplitude decreases, it remains above the yield strength of the material, as displayed in Fig. 29(d). By the end of penetration, the stress level in the charge reduces to 40.6 MPa, as shown in Fig, 29(e). Throughout the process, the stress distribution characteristics and amplitudes in the *xoy* and *yoz* planes remain consistent, with the stress level in the charge sustained above the yield strength of the material for an extended period, indicating irreversible plastic deformation in addition to elastic deformation.

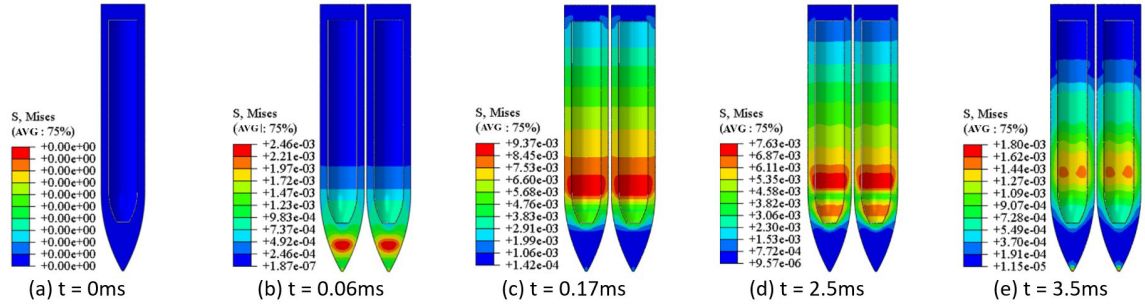

Figure 28 Shell equivalent force evolution process

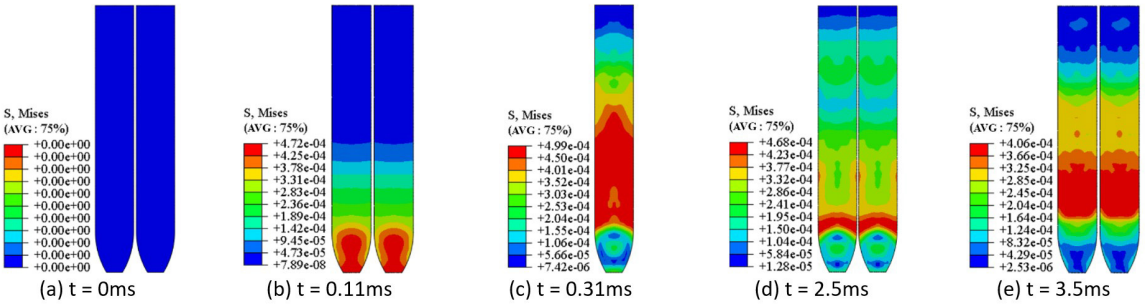

Figure 29 Charge equivalent force evolution process

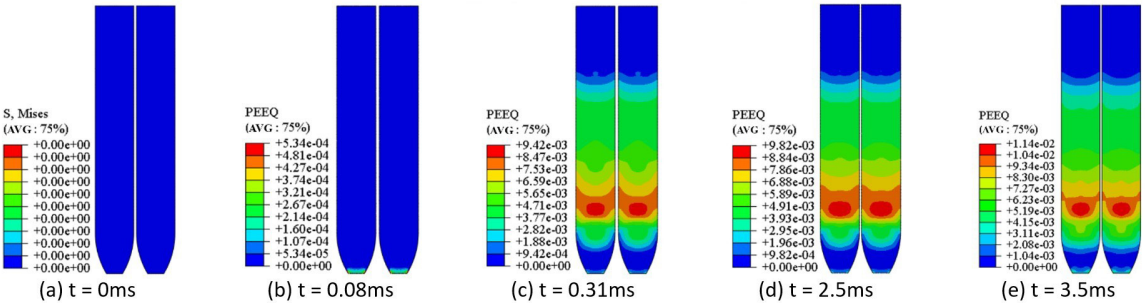

Figure 30 Equivalent plastic strain cloud for charge

Under positive penetration conditions, the plastic deformation of the shell head is negligible; therefore, only the equivalent plastic strain evolution process of the charge is presented. The characteristics of plastic strain distribution and stress propagation processes are shown in Fig. 30. The charged nose is subjected to a strong compression wave after the impact. The charge nose exhibits the earliest evidence of plastic deformation at 0.08 ms, with an amplitude of 5.34×10^{-4}, as shown in Fig. 30(b). As the penetration continues, a concentrated plastic strain region develops approximately 1/3 times of the charge length from the head, with the strain amplitude reaching 0.0094. By 2.5 ms, the maximum plastic strain amplitude in the charge rises, and the high-strain area expands, as illustrated in Figs. 30(c) and 30(d). At 3.5 ms, the charge

equivalent plastic strain reaches 0.0114, concentrated along the charge's head sideline. At this stage, the curvature of the warhead shell and the charging head directs the stress wave toward the charge axis, forming a high-strain region near the axis in the charge's forward section, as depicted in Figs. 30(c)–(e).

To further analyze the kinetic response of the internal charge, representative units were selected. Units from the axis to the edge were selected as representatives of the nose cross-section, between the head and columnar segments, and half the charge length. These units enabled the extraction of axial stress along the longitudinal axis and the time-course curve of axial stress distribution along the loading axis.

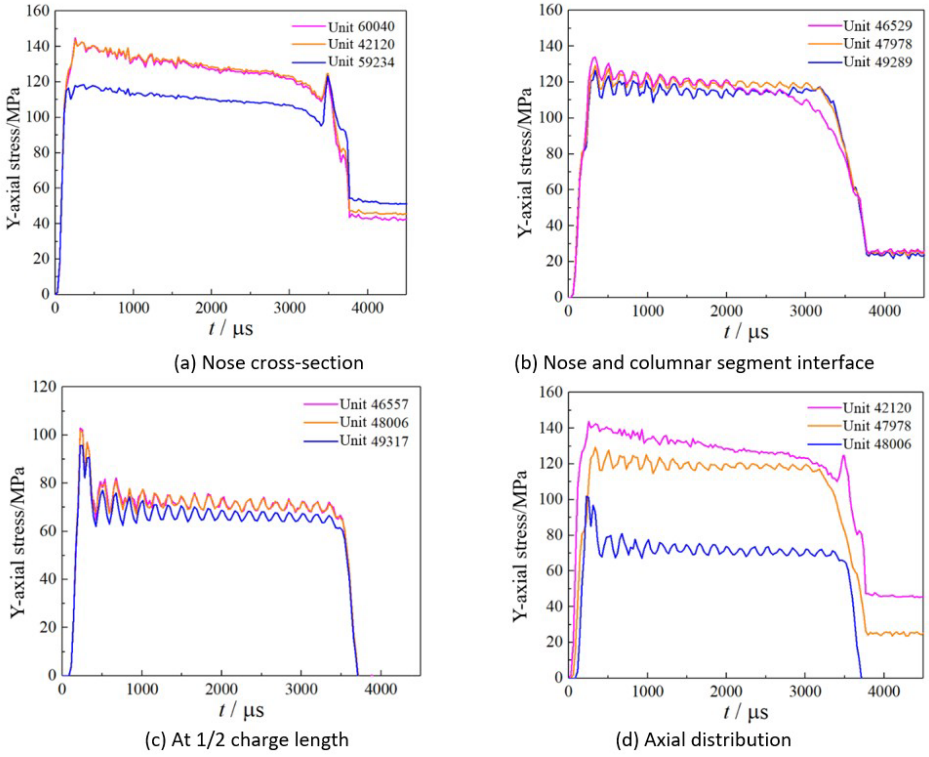

Figure 31 Axial stresses in the unit at different positions of the long axis profile

Fig. 31 demonstrates that axial stress increases progressively along the radial direction from the edge to the interior of the charge. In contrast, axial stress decreases along the longitudinal direction from the front to the rear of the charge. This pattern occurs because, during penetration, the ogive-shaped projectile shell makes initial contact with the concrete target along the symmetry axis. Therefore, axial stresses are higher within the charge than at its edges. Additionally, the stress wave amplitude diminishes during axial propagation, leading to higher axial stress at the charge's nose compared to its midpoint.

The charge also experiences shear forces, with the time-dependent shear stress curve in the *xoy* plane of the cell shown in Fig. 32. It can be observed that the shear stress in internal units at various positions remains low, indicating limited susceptibility to shear deformation near the charge symmetry axis. Moving radially outward from the charge interior to its edge, shear stress increases, suggesting that the edge units of the charge are more prone to shear deformation. Furthermore, as seen in Fig. 32(d), shear stress decreases along the axial direction from the charge's front end to its rear, indicating that shear deformation is most pronounced along the charge nose's edge.

Cross-sectional strain contour plots at the charge nose's end face, the interface between the nose and columnar section, and at the midpoint of the charge are shown in Fig. 33. The strain distribution along the radial and axial directions is depicted in Fig. 34. From the figures, it is evident that strains at the nose's end face and at the interface between the nose and columnar segment are uniformly distributed along the axial direction. Equivalent plastic strain in the charge nose shows an increasing trend from the symmetry axis outward to the edges in the radial direction under shear forces, regardless of whether the long or short axis is considered. Equivalent plastic strain in the cross section at the interface between the head and columnar section, as well as at the charge midpoint, displays a decreasing trend from the symmetry axis outward, with strain rising again at the edge due to shear stress.

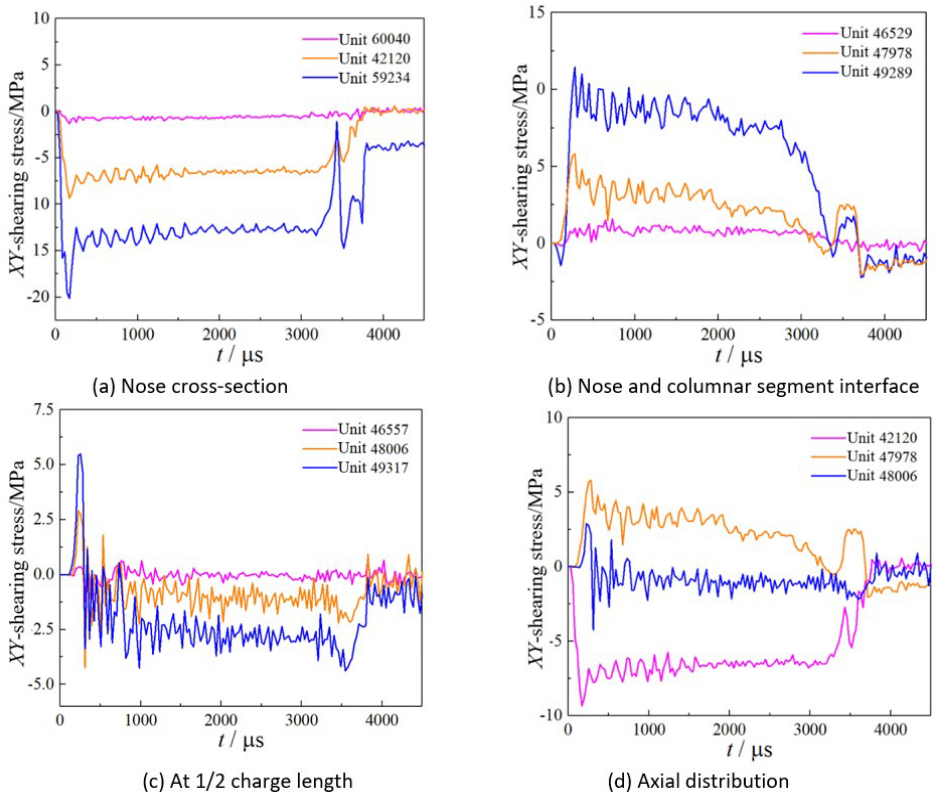

Figure 32 Axial stresses in the cell at different locations in the profile

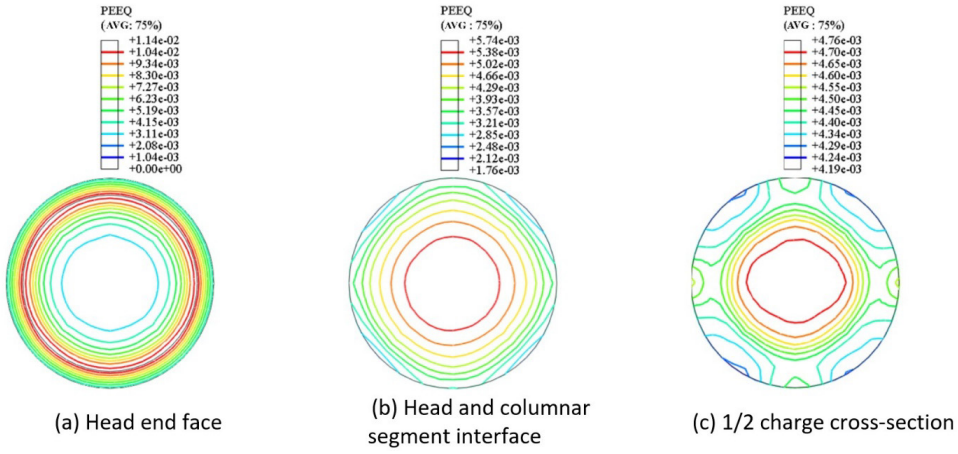

Figure 33 Contour plots of cross sectional strains at different locations of the charge

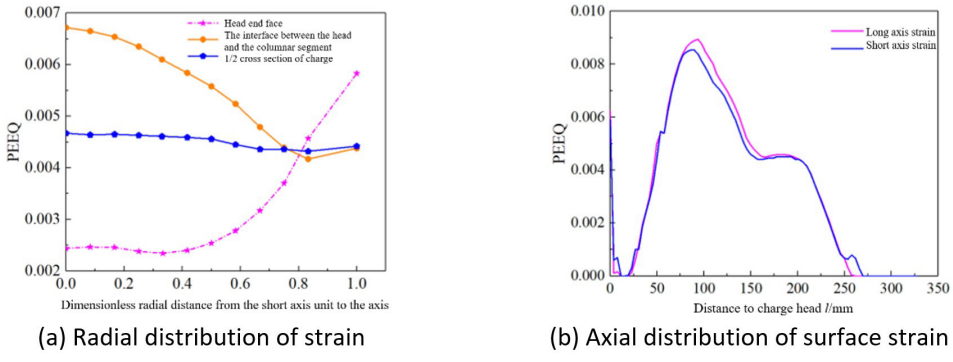

Figure 34 Distribution of loading strain

4 CONCLUSION

Penetration experiments were conducted using a 30-mm ballistic gun to analyze projectile penetration into concrete targets. The dynamic response characteristics of the projectiles were carefully observed. Using a numerical simulation method for projectile-target separation, a model was established to simulate projectile penetration into concrete, allowing for a detailed analysis of the dynamic responses of both the projectile and the charge under various conditions. The primary conclusions are as follows:

(1) A resistance model for projectile penetration into concrete was modified based on experimental measurements of crater parameters. Using a projectile–target separation simulation method, the projectile deformation process was analyzed, achieving less than a 10% error between calculated and experimental results.

(2) During oblique penetration into the target, the projectile nose experiences substantial compression due to the compression wave, resulting in pronounced deformation between 0.32 and 0.59 times the projectile length from the nose. Compression and tensile waves combine to produce significant transverse deformation at the projectile's rear, specifically in the region spanning 0.88 to 1.0 times the projectile length from the tail.

(3) Axial stress in the projectile increases progressively from the charge's edge toward its interior and then decreases along the axial direction from the front to the rear of the charge. Axial stress is higher at the charge head than at the midpoint along the charge length.

Acknowledgments

This research is supported by the National Natural Science Foundation of China (Nos. 12202205 and 12141202).

Author's Contribuitions: Conceptualization, Changlin Zhu and Chuang Liu; Methodology, Qiang Sheng; Investigation, Yuxuan Deng; Writing - original draft, Changlin Zhu and Chuang Liu; Writing - review & editing, Xiaoming Wang; Funding acquisition, Chuang Liu; Resources, Changlin Zhu and Chuang Liu; Supervision, Xiaoming Wang.

Data availability: Research data is only available upon request

Editor: Marcílio Alves

References

Bi C, Guo X, Qu K P, et al. (2022)Numerical simulation of charge damage during oblique penetration. Chinese Journal of Explosives & Propellants, 45(3):383-387.

Chen X, Zhang D, Yao S, et al. (2017)Fast algorithm for simulation of normal and oblique penetration into limestone targets. Applied Mathematics and Mechanics, 38: 671-688.

Deng J J, Zhang X F, Chen D D, et al. (2016)Numerical simulation of the trajectory of travelling projectile penetrating into pre-drilled target. Acta Armamentarii, 37(5): 808-816.

Deng J J. (2018)Study on the penetration mechanism of grooved-nose projectile impact to concrete target. Nanjing: Nanjing University of Science and Technology.

Du H C. (2021)Study on the trajectory characteristics of oblique penetration of asymmetrical grooved-nose projectile into typical target. Nanjing: Nanjing University of Science and Technology.

Fang Q, Kong X, Hong J, et al. (2014)Prediction of projectile penetration and perforation by finite cavity expansion method with the free-surface effect. Acta Mechanica Solida Sinica, 27(6): 597-611.

Forrestal M J, Longcope D B. (1990)Target strength of ceramic materials for high-velocity penetration. Journal of Applied Physics, 67(8): 3669-3672.

He T. (2007)A Study on the Penetration of Projectiles intoTargets Made of Various Materials. University of Science and Technology of China.

Kong X Z, Fang Q, Wu H. (2014)Terminal ballistics study of deformable projectile penetrating brittle material targets for free-surface and crack region effects. Acta Armamentarii, 35(6): 814-821.

Li D C, Chen Li, Ding Y S. (2009)A model of explosioninduced by frictioninthe process of loaded projectiles penetration into concrete targets. Explosive and Shock Waves, 29(01): 13-17.

Li P C, Zhang X F, Liu C, et al. (2024)Trajectory characteristics of oblique penetration of projectile into concrete targets considering cratering effect. International Journal of Impact Engineering, 185: 104864.

Li P C, Zhang X F, Wang GJ, et al. (2023)Dynamic cratering process during penetration of rigid projectile into concrete target. Explosion and Shock Waves, 43(9): 091402.

Li X, Liu Y Z, Sun Y. (2020)Dynamic mechanical damage and non-shock initiation of a new polymer bonded explosive during penetration. Polymers, 12(6).

Li Y C. (2021)Study on dynamic response of charge projectile under high impact. North University of China.

Ng E G, El-Wardany T I, Dumitrescu M, et al. (2002)Physics-based simulation of high speed machining. Machining Science and Technology, 6(3): 301-329.

Shi X H, Yu C X, Dai K D, et al. (2019)The influence of nose shape to dynamic damage of PBX charge during the penetration process.Journal of Projectiles, Rockets, Missiles and Guidance.

Warren T L, Forquin P. (2016)Penetration of common ordinary strength water saturated concrete targets by rigid ogive-nosed steel projectiles[J]. International Journal of Impact Engineering, 90: 37-45.

Warren T L, Tabbara M R. (2000)Simulations of the penetration of 6061-T6511 aluminum targets by spherical-nosed VAR 4340 steel projectiles. International journal of solids and structures, 37(32): 4419-4435.

Xu W Z, Wang J Y, Li J L, et al. (2011)Theovetical analysis and simulation for penetration overload of a small size charge. Journal of Vibration and Shock, 30(07):96-100.

Yoo Y H, Kim J B, Lee C W. (2019)Effects of the projectile geometries on normal and oblique penetration using the finite cavity pressure method. Applied Sciences, 9(18): 3939.

Zhang B, Li J C, Chen J L, et al. (2023)Loading characteristics and structural response of a warhead during drop impact. Explosion And Shock Waves, 43(3): 033201.

Zhang X, Cao R Y, Tan D W. (2011)Plastic Charge Stability Analysis of Supersonic Projectile During Penetration of Concrete Targets. Chinese Journal of Energetic Materials, 19(6):709-714.

Zhang X Y, Wu Y Q, Hang F L. (2018)Numerical simulation on the dynamic damage of PBX charges filled in projectiles during penetrating thin concrete targets. Chinese Journal of Energetic Materials, 26(1):101-108.contri